A new analytical model of the cosmic-ray energy flux for Galactic diffuse radio emission

Andrea Bracco, Marco Padovani, Daniele Galli

A&A, 686, A52 (2024)
https://doi.org/10.1051/0004-6361/202449625

Astronomy & Astrophysics

A new analytical model of the cosmic-ray energy flux for Galactic diffuse radio emission⋆

Andrea Bracco[1,2], Marco Padovani[1], and Daniele Galli[1]

[1] INAF – Osservatorio Astrofisico di Arcetri, Largo E. Fermi 5, 50125 Firenze, Italy
e-mail: andrea.bracco@inaf.it
[2] Laboratoire de Physique de l'Ecole Normale Supérieure, ENS, Université PSL, CNRS, Sorbonne Université, Université de Paris, 75005 Paris, France

Received 15 February 2024 / Accepted 29 February 2024

ABSTRACT

Low-frequency radio observations of diffuse synchrotron radiation offer a unique vantage point from which to investigate the intricate relationship between gas and magnetic fields in the formation of structures within the Galaxy, spanning from the diffuse interstellar medium (ISM) to star-forming regions. Achieving this pivotal objective hinges on a comprehensive understanding of cosmic-ray properties; these dictate the effective energy distribution of relativistic electrons, which are primarily responsible for the observable synchrotron radiation. Notably, cosmic-ray electrons (CRe) with energies of between 100 MeV and 10 GeV play a crucial role in determining the majority of the sky brightness below the GHz range. However, their energy flux (j_e) remains elusive because of solar modulation. We propose a way to derive observational constraints on this energy gap of interstellar CRe through the brightness temperature spectral index of low-frequency radio emission, here denoted β_{obs}. We introduce a new parametric analytical model that fits available data for j_e in accordance with the β_{obs} values measured in the literature between 50 MHz and 1 GHz for diffuse emission in the Milky Way. Our model accounts for multiple observations considering magnetic-field strengths consistent with existing measurements below 10 μG. We present a first all-sky map of the average component of the magnetic field perpendicular to the line of sight and validate our methodology against state-of-the art numerical simulations of the diffuse ISM. This research makes headway in modeling Galactic diffuse emission with a practical, parametric form. It provides essential insights that will help preparations for the imminent arrival of the Square Kilometre Array.

Key words. magnetic fields – radiation mechanisms: non-thermal – cosmic rays – ISM: general – ISM: magnetic fields

1. Introduction

Low-frequency radio emission observations are paving the way for a comprehensive study of Galactic magnetic fields traced by synchrotron radiation. The breakthrough in sensitivity achieved by current and upcoming radio telescopes, including the Low Frequency Array (LOFAR, van Haarlem et al. 2013), the Long Wavelength Array (LWA, Dowell et al. 2017), the New Extension in Nançay Upgrading LOFAR (NenuFAR, Zarka et al. 2012), the C-Band All-Sky Survey (Jones et al. 2018), and the Square Kilometre Array (SKA, Dewdney et al. 2009), along with its precursors, promises a highly detailed multiscale description of the Galactic magnetic field. This description will encompass both its topology and its strength, ranging from the diffuse interstellar medium (ISM) to star-forming regions (Heald et al. 2020).

However, achieving this paramount objective will require a thorough characterization of cosmic-ray (CR) properties, and deep understanding of their acceleration and propagation. These factors determine the effective energy distribution of relativistic electrons, which are primarily responsible for the observable synchrotron radiation[1] (e.g., Ginzburg & Syrovatskii 1964; Padovani & Galli 2018). In particular, low-energy cosmic-ray electrons (CRe) between 100 MeV and 10 GeV are those relevant for most of the radio emission detected below the GHz range (Padovani et al. 2021, hereafter P21). Unfortunately, because of solar modulation, the energy flux of these electrons (j_e) cannot be measured from near-earth direct observations (e.g., Gabici 2022). Hence, j_e is usually interpolated in the GeV window (e.g., Orlando 2018; Padovani & Galli 2018; Padovani et al. 2018; Unger & Farrar 2024; Bracco et al. 2023) between the MeV range observed with the Voyager spacecrafts (Cummings et al. 2016; Stone et al. 2019) and the hundreds-of-GeV range measured by facilities including *Fermi*-LAT (Ackermann et al. 2010), Pamela (Adriani et al. 2011), and the Alpha Magnetic Spectrometer (AMS, Aguilar et al. 2014).

Building upon the pioneering works of Rockstroh & Webber (1978), Strong & Wolfendale (1978), and Strong et al. (2000), and following up on the investigation conducted by P21, in the present paper we propose that observational constraints on the missing energy window of interstellar CRe can be obtained through the spectral index of low-frequency radio emission, denoted β_{obs}. We introduce a new analytical-parametric model that accurately fits j_e whilst considering the values of β_{obs} measured in the literature between 45 MHz and 408 MHz for Galactic diffuse emission. We use our models of j_e to estimate the strength of the Galactic magnetic field averaged along the line of sight (LOS). Our observational results are discussed through a comparison with synthetic data generated from state-of-the-art magneto-hydrodynamic (MHD) simulations of the diffuse ISM.

By incorporating the constraint of β_{obs} in the shape of j_e, we demonstrate an enhanced ability to statistically account for numerous observations between 50 MHz and 1 GHz. This

⋆ The map displayed as Fig. 4 is available at the CDS via anonymous ftp to cdsarc.cds.unistra.fr (130.79.128.5) or via https://cdsarc.cds.unistra.fr/viz-bin/cat/J/A+A/686/A52

[1] Positrons and secondary electrons also contribute to synchrotron radiation but at a few % level (Orlando 2018; Ponnada et al. 2024).

improvement is achieved without resorting to unrealistic values for the strength of the Galactic magnetic field, which, as measured through Zeeman splitting in the diffuse ISM and rotation measures of pulsars, averages less than 10 μG (Heiles & Troland 2005; Sobey et al. 2019). This research represents a notable advancement in the modeling of Galactic diffuse emission, offering crucial insights that will help to prepare for the arrival of the SKA.

The paper is organized as follows: in Sect. 2, we introduce the basic formalism of synchrotron emission and review several observations of $\beta_{\rm obs}$ at low frequencies reported in the literature; in Sect. 3, we present our $j_{\rm e}$ model; in Sect. 4, we derive an all-sky map of the magnetic-field strength and validate our methodology with MHD simulations. In Sect. 5, we provide a discussion of our findings and in Sect. 6 we summarize our conclusions.

2. Observations of the synchrotron spectral index

In this section, we first introduce the formalism linking $j_{\rm e}$ and $\beta_{\rm obs}$ (Sect. 2.1) and then summarize the observed values of $\beta_{\rm obs}$ below 1 GHz (Sect. 2.2). We provide a list of observational results that is not intended to be comprehensive but rather representative of what can be found in the literature.

2.1. From first principles to brightness temperature

Galactic synchrotron diffuse emission arises from the interaction of interstellar magnetic fields with CRe (e.g., Ginzburg & Syrovatskii 1964; Rybicki & Lightman 1979). These relativistic particles gyrate about the field lines emitting nonthermal radiation dependent on their energy (E) and the magnetic-field strength perpendicular to the sightline ($B_\perp = |\boldsymbol{B}_\perp|$). The total synchrotron emissivity in units of power per unit volume, frequency (ν), and solid angle is the sum of the emissivities linearly polarized along ($\varepsilon_{\nu,\parallel}$) and across ($\varepsilon_{\nu,\perp}$) $\boldsymbol{B}_\perp$:

$$\varepsilon_{\nu,\parallel}(\boldsymbol{r}) = \int_{m_{\rm e}c^2}^{\infty} \frac{j_{\rm e}(E)}{v_{\rm e}} P^{\rm em}_{\nu,\parallel}(E, B_\perp(\boldsymbol{r}))\,{\rm d}E \qquad (1)$$
$$\varepsilon_{\nu,\perp}(\boldsymbol{r}) = \int_{m_{\rm e}c^2}^{\infty} \frac{j_{\rm e}(E)}{v_{\rm e}} P^{\rm em}_{\nu,\perp}(E, B_\perp(\boldsymbol{r}))\,{\rm d}E,$$

where $v_{\rm e}$ is the CRe velocity, $m_{\rm e}$ is their mass, c is the speed of light, $\boldsymbol{r}$ is the position, and $P^{\rm em}_{\nu,\perp\ {\rm or}\ \parallel}$ is the power per unit frequency for the two polarizations (see also Eq. (2) in P21 and Longair 2011). By integrating Eq. (1) along the LOS, and accounting for the telescope beam ($\Theta_{\rm T}$), one obtains the synchrotron brightness temperature as

$$\frac{T_{\rm b}(\nu)}{[{\rm K}]} = \frac{2\ln(2)\, c^2 10^{-23}}{\pi k_{\rm B} \theta_{\rm T}^2 \nu^2} \left[\Theta_{\rm T} \circledast \int_{\rm LOS} (\varepsilon_{\nu,\parallel} + \varepsilon_{\nu,\perp}) {\rm d}r\right], \qquad (2)$$

where $k_{\rm B}$ is the Boltzmann constant and the $\circledast$ symbol represents the convolution with a Gaussian-approximated $\Theta_{\rm T}$ given its full width at half maximum (FWHM), $\theta_{\rm T}$, in units of radians. Observationally, $T_{\rm b}(\nu)$ mostly results in a power-law function of ν with spectral index $\beta_{\rm obs}$ (e.g., Reich & Reich 1988a,b; Roger et al. 1999). From Eqs. (1) and (2), and as already shown by P21, the value of $\beta_{\rm obs}$ is not expected to be constant but rather to vary depending on the MHD properties of the intervening ISM and on $j_{\rm e}$. Notably, it has long been known that energy losses may contribute to modifying the synchrotron spectral index, as illustrated by several observations at low frequencies in the radio band (e.g., Bridle 1967; Sironi 1974; Webster 1975) as well as by diffusion and convection models of CRe propagation (e.g., Strong 1977).

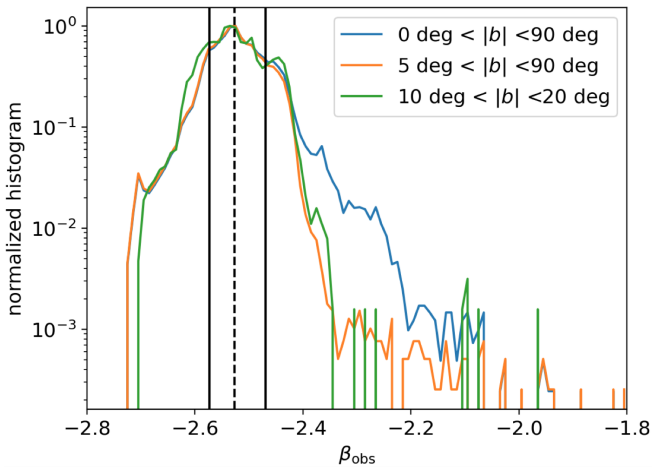

Fig. 1. Normalized histograms of the observed spectral indices, $\beta_{\rm obs}$, between 45 MHz and 408 MHz from G11 as a function of Galactic latitude. The 50th, 16th, and 84th percentiles of the orange histogram are marked in black dashed and solid lines, respectively.

In this work, we exploit these dependencies and invert the argument using ancillary observations of $\beta_{\rm obs}$ to constrain $j_{\rm e}$ and $B_\perp$. In the following, we distinguish the observed values of the spectral index, $\beta_{\rm obs}$, from those derived from models, denoted $\beta_{\rm syn}$.

2.2. Observed spectral indices below 1 GHz

Measurements of the synchrotron spectral index from diffuse emission in the Galaxy generally vary between −2 and −3 depending on the observed frequency range, the sky coverage, and the FWHM of the instrument. Most $\beta_{\rm obs}$ at frequencies below 408 MHz were recently measured with single-dipole antennas designed for low-frequency cosmological experiments, such as the Experiment to Detect the Global EoR Signature (EDGES, Bowman et al. 2008) and the Large-Aperture Experiment to Detect the Dark Ages (LEDA, Price et al. 2018). These experiments measured $-2.59 < \beta_{\rm obs} < -2.54$ between 50 MHz and 100 MHz (Mozdzen et al. 2019), $-2.62 < \beta_{\rm obs} < -2.60$ between 90 MHz and 190 MHz (Mozdzen et al. 2017), and $-2.55 < \beta_{\rm obs} < -2.45$ between 50 MHz and 87 MHz (Spinelli et al. 2021). While these measurements integrate the synchrotron flux over the full accessible sky, higher angular resolution observations of $\beta_{\rm obs}$ are also available. In particular, in this work we refer to one of the all-sky $\beta_{\rm obs}$ maps of reference for low-frequency studies derived by Guzmán et al. (2011), hereafter G11, between 45 MHz and 408 MHz using data from Alvarez et al. (1997), Maeda et al. (1999), and Haslam et al. (1982)[2]. This map, with a FWHM of 5 degrees, shows large variations of $\beta_{\rm obs}$ ranging between −2.7 and −2.1. In Fig. 1, we show the normalized histograms of these $\beta_{\rm obs}$ as a function of Galactic latitude (b). Most of the shallow values of $\beta_{\rm obs}$ are confined to the Galactic plane, $|b| < 5°$ (compare the blue and orange curves), which is possibly due to free-free absorption of radio photons along the LOS (e.g., Stanislavsky et al. 2023). However, the distribution of the values of $\beta_{\rm obs}$ at intermediate to high Galactic latitudes above

[2] The map can be downloaded at the following link: http://cdsarc.u-strasbg.fr/viz-bin/qcat?J/A+A/525/A138

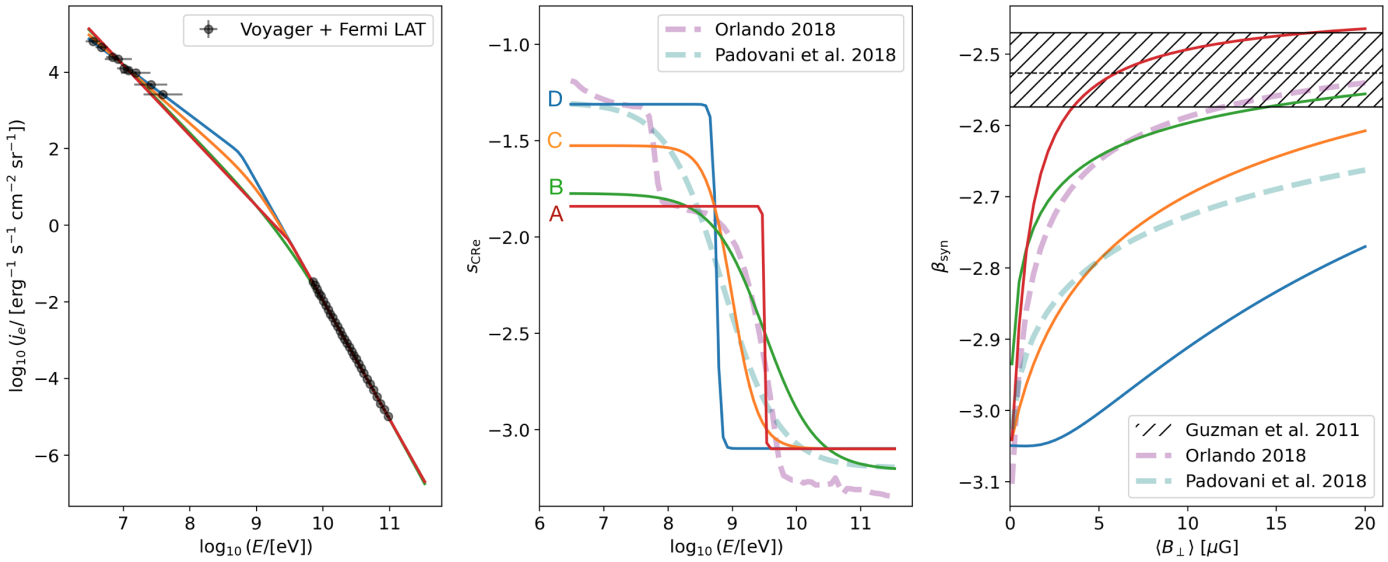

Fig. 2. Our models for s_{CRe} obtained with Eq. (3) and their impact on the modeled synchrotron spectral index β_{syn}. Colors correspond to the same models in all panels. *Left panel*: j_e from models A, B, C, and D with parameters listed in Table 1 that fit the black data points from Voyager ($E < 10^8$ eV, Cummings et al. 2016; Stone et al. 2019) and *Fermi*-LAT ($E > 10^{10}$ eV, Ackermann et al. 2010). *Central panel*: s_{CRe} values corresponding to the same models as in the left panel. *Right panel*: values of β_{syn} for the same models as in the other panels with the observed spectral indices from G11 in hatches – the 16th, 50th, and 84th percentiles are marked as in Fig. 1. Models for s_{CRe} and β_{syn} using j_e from Orlando (2018) and Padovani et al. (2018) are also shown in dashed purple and teal lines in the central and right panels, respectively.

$|b| > 5°$ is stable with a rather normal shape (see the green and orange curves). The 50th, 16th, and 84th percentiles of the orange histogram are −2.53, −2.57, and −2.47, respectively.

More recent all-sky maps at the degree-scale level, depicting β_{obs} values from 35 MHz to 80 MHz, are available from the LWA (Dowell et al. 2017). These maps closely agree with those presented by G11, although they display slightly shallower β_{obs} values at intermediate Galactic latitudes. The authors did not extensively investigate these differences, attributing them to (*i*) variations in frequency coverage and (*ii*) residual systematic effects present in their data.

Remarkably, β_{obs} maps of external galaxies, such as NGC 5775 and NGC 891, have been produced at low frequency with LOFAR and the Very Large Array (Mulcahy et al. 2018; Heald et al. 2020). We note that, in both cases, the maps appear consistent with the β_{obs} map of G11 outside of their galactic halo.

At higher frequencies, above 408 MHz, the β_{obs} values for diffuse Galactic emission typically converge towards −3. A recent example of this comes from the analysis of MeerKAT data (with FWHM of approximately 1 degree) between 971 MHz and 1075 MHz at intermediate Galactic latitudes, which yielded an average β_{obs} value of -2.76 ± 0.15 (Irfan et al. 2022, and references therein).

3. Modeling the CRe energy flux

The ability of models to reproduce the observed synchrotron sky brightness and β_{obs} strongly relies on the choice of j_e and its approximations (see Eq. (1)). As discussed in P21, most theoretical models and numerical simulations of Galactic synchrotron emission assume fixed power laws for the energy distribution of CRe depending on the frequency range (e.g., Sun et al. 2008; Waelkens et al. 2009; Sathyanarayana Rao et al. 2017; Reissl et al. 2019; Wang et al. 2020). However, this assumption may lead to significant biases in the interpretation of synchrotron data, notably concerning the spatial variations of the spectral index at both low and high frequency. The energy dependence of the slope of j_e between 100 MeV and 50 GeV should be taken into account.

Some effort has been made in this direction, as shown for instance by the works by Padovani et al. (2018) and Orlando (2018). The former proposed an analytical four-parameter model that reproduces the power-law behavior of j_e measured at low and high energies (see Sect. 1). The latter is based on a combination of multifrequency observations, Voyager measurements, and the CRe propagation code called GALPROP (e.g., Porter et al. 2022, for a recent release). However, as shown with dashed lines in the right panel of Fig. 2, both cases struggle to reproduce the range of β_{obs} described in Sect. 2.2 (see hatches from G11)[3] without resorting to improbably large values for the average $B_\perp$ along the LOS (hereafter, $\langle B_\perp \rangle$), that is, of the order of 20 µG.

In this context, we propose a new analytical model for j_e tailored to capture its variation in the energy gap encompassing 1 GeV. We introduce a four-parameter model that describes the logarithmic derivative of j_e with respect to E (s_{CRe}), as follows:

$$s_{\mathrm{CRe}} = \frac{\mathrm{d}\log_{10} j_e}{\mathrm{d}\log_{10} E} = \frac{s_1 - s_2}{1 + (E/E_0)^\gamma} + s_2, \tag{3}$$

where $\gamma = 1/\log(\Delta E/[\mathrm{eV}])$, and ΔE represents the energy range around E_0 at which the transition between the low-energy and high-energy slopes, s_1 and s_2, occurs. For comparison, the s_{CRe} curves from Orlando (2018) and Padovani et al. (2018) are displayed in the central panel of Fig. 2.

[3] We note that Orlando (2018) developed their j_e model including the radio data employed by G11. However, since their post-processing was not the same, in particular concerning their methods of component separation (i.e., thermal and nonthermal components), the respective β_{obs} are different. We choose to consider the work of G11, as it is widely referred to in the radio community at low frequency. It is beyond our scopes to discuss at length the inconsistencies between these two works.

Table 1. Model parameters entering Eq. (3) and shown in Figs. 2 and 6.

Model	s_1	s_2	E_0 (GeV)	γ	Region
A	−1.8	−3.1	3.2	45	Diffuse ISM
B	−1.8	−3.2	3.2	2.2	Diffuse ISM
C	−1.5	−3.1	1	1.1	Diffuse ISM
D	−1.3	−3.1	0.6	14	Diffuse ISM
E	−1.2	−3.1	3.2	45	Orion-Taurus ridge

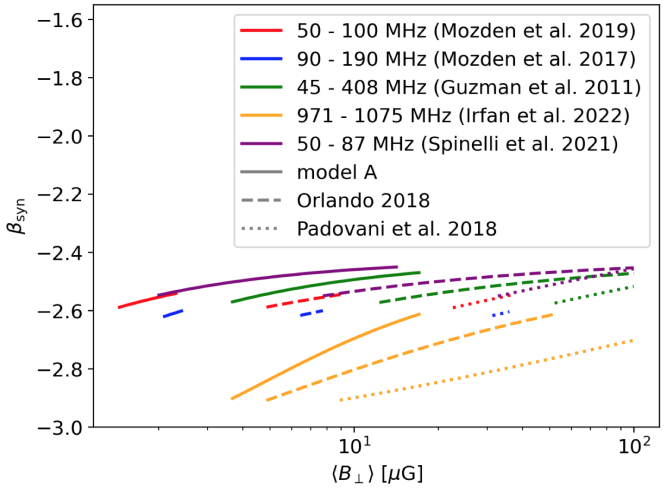

Fig. 3. Modeled synchrotron spectral indices, β_{syn}, reproducing various observational results of β_{obs} (in different colors) with model A (solid lines), Orlando (2018, dashed lines), and Padovani et al. (2018, dotted lines). Data are the following: 50–100 MHz (red), and 90–190 MHz (blue) using EDGES (Mozdzen et al. 2017, 2019); 45–408 MHz using a set of multiple observations (G11); 971–1075 MHz using MeerKAT (Irfan et al. 2022); 50 and 87 MHz using LEDA (Spinelli et al. 2021).

Instead of fitting the full set of independent data at once (from those of j_e to the radio ones) to illustrate the impact of our parameters, in Fig. 2, we show four realizations of our model that correspond to models A to D in Table 1.

From left to right, models are shown with the same color for j_e, s_{CRe}, and β_{syn}, respectively. Despite all fitting the Voyager and *Fermi*-LAT data in the left panel, they behave differently in the 1 GeV energy window, as depicted in the central panel. This energy range determines the observable brightness and the corresponding β_{syn}, as illustrated in the right panel. Model A, characterized by a sharp change in slope of j_e at about 3 GeV (not distinguishable from a step function in s_{CRe}), is the type of model that converges in both energy and frequency for values of $\langle B_\perp \rangle$ below 10 μG. Our approach is purely phenomenological and, on average, suggests the existence of two power laws of CRe contributing to synchrotron emission.

Using model A as a reference, in Fig. 3, we also compare our estimates of β_{syn} with the models of Padovani et al. (2018) and Orlando (2018) for a number of observations below 1 GHz (see Sect. 2.2). As for the range of β_{obs} from G11, we show that model A better reproduces β_{obs} at both low and high frequency for realistic values of $\langle B_\perp \rangle < 10$ μG. We note that most single-dipole-antenna experiments produce β_{obs} values that are consistent with smaller $\langle B_\perp \rangle$ than other instruments. This is possibly due to averaging Galactic diffuse emission and $B_\perp$ over larger sky areas.

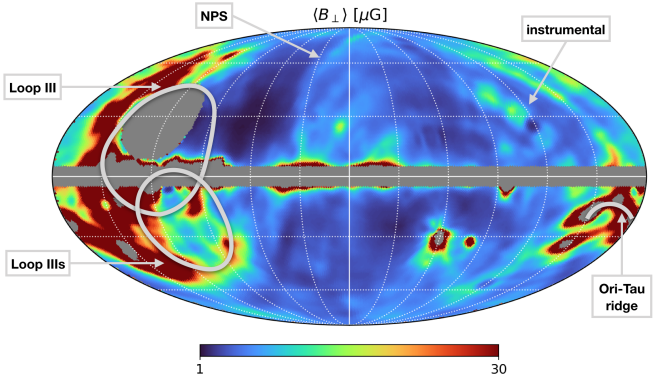

Fig. 4. Map of the plane-of-the-sky magnetic-field strength averaged along the LOS, $\langle B_\perp \rangle$, derived with β_{obs} from G11 (see orange histogram in Fig. 1) and assuming a spatially uniform j_e described by model A. We label one possible instrumental pattern and a few known radio structures: the Orion-Taurus ridge (Ori-Tau ridge, Bracco et al. 2023), the North Polar Spur (NPS), Loop III, and Loop IIIs (e.g., Vidal et al. 2015). A Galactic coordinate grid is overlaid that is centered on the Galactic center with steps of 30° in latitude and longitude.

4. Estimate of the magnetic-field strength

Assuming model A for j_e, in this section we derive a map of $\langle B_\perp \rangle$ from the β_{obs} map of G11 (Sect. 4.1). We compare these results with synthetic data of synchrotron diffuse emission (Sect. 4.2).

4.1. All-sky $\langle B_\perp \rangle$ map from β_{obs} between 45 and 408 MHz

In the previous sections, we demonstrate that model A is capable of statistically reproducing the correct values of β_{obs} observed at intermediate-to-high Galactic latitudes, both by fitting the available j_e data and for values of $\langle B_\perp \rangle$ lower than 10 μG. With this model, we utilize the corresponding functional form of β_{syn} – which is dependent on $\langle B_\perp \rangle$, as depicted in red in the right panel of Fig. 2 – to interpolate the β_{obs} map presented in G11 and infer the respective map of $\langle B_\perp \rangle$.

The resulting all-sky map is displayed in Fig. 4, shown with a linear scale between 1 μG and 30 μG. A circular region around the north celestial pole is masked as in G11. We note that most of the sky above $|b| > 5°$ is consistent with values of $\langle B_\perp \rangle$ below 15 μG, as expected from Sect. 3. This suggests that, over most of the diffuse sky, considering a uniform spatial distribution of j_e to describe the energy flux of CRe is a reasonable assumption.

However, a few regions stand out on the map. On one hand, some striped patterns to the west may be associated with instrumental artifacts present in the G11 map. On the other hand, most of the notable structures correspond to well-known arcs in the radio sky, such as the Orion-Taurus ridge (Ori-Tau ridge, Planck Collaboration XXV 2016; Bracco et al. 2023), the North Polar Spur (NPS), and Loops III–IIIs (e.g., Vidal et al. 2015). In Sect. 5, we discuss possible reasons that could explain their particular appearance on the map with values of $\langle B_\perp \rangle$ significantly larger than 15 μG. Finally, some residual contamination of free-free absorption in the proximity of the Galactic plane could bias the estimate of $\langle B_\perp \rangle$ toward large values (e.g., between Galactic longitudes, $-30° < l < +30°$).

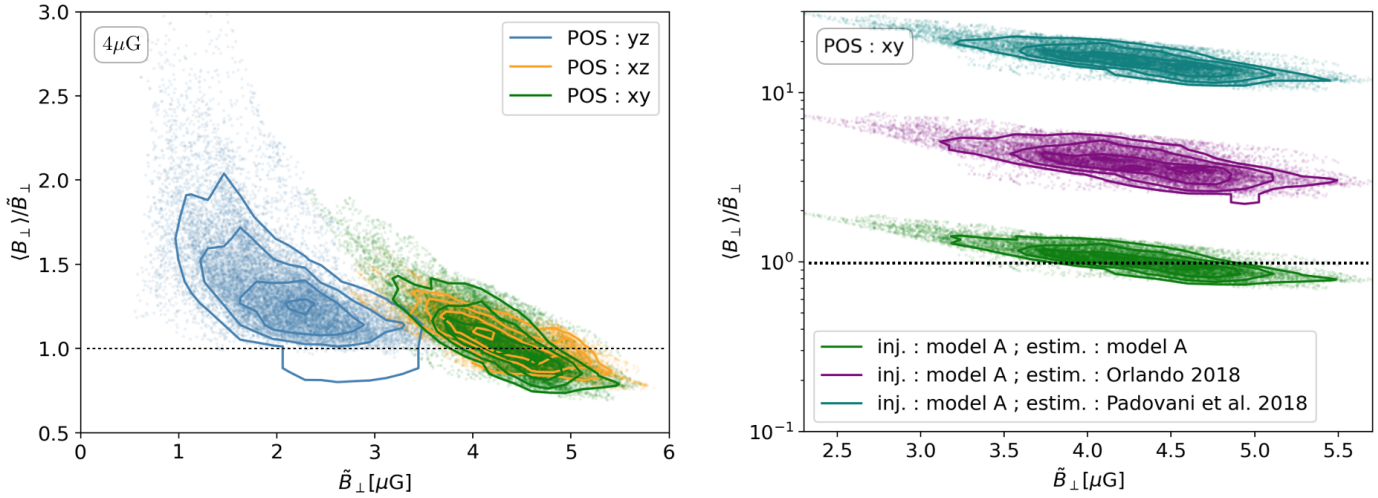

Fig. 5. Estimate of $\langle B_\perp \rangle$ using synthetic intensity data at 45 and 408 MHz obtained with model A from one MHD simulation (Bellomi et al. 2020) already implemented in P21 to study diffuse Galactic synchrotron emission. The initial mean magnetic-field strength of the simulation is 4 μG. The value of $\langle B_\perp \rangle$ is estimated as in Fig. 4. *Left panel*: ratio between the estimated $\langle B_\perp \rangle$ and the true median value of the plane-of-the-sky magnetic-field strength per pixel, $\tilde{B}_\perp$, shown as a function of $\tilde{B}_\perp$ for the three integration axes. *Right panel*: for the green case shown in the left panel, given the injected j_e-shape of model A in the simulations, $\langle B_\perp \rangle$ is also estimated using presently existing models; i.e. Orlando (2018, in purple) and Padovani et al. (2018, in teal). In all panels the, levels show the (0.5, 1, 1.5, 2)σ equivalent contours of the corresponding density of points.

4.2. Validation of the $\langle B_\perp \rangle$ map with synthetic data

We validate the methodology used to derive the $\langle B_\perp \rangle$ map using synthetic data of synchrotron emission at 45 MHz and 408 MHz obtained from one state-of-the-art MHD numerical simulation of the multiphase and magnetized ISM (Bellomi et al. 2020). In summary, this numerical model, generated using the RAMSES code (Teyssier 2002; Fromang et al. 2006), simulates a 50 pc cube with 128 pixels per side of warm diffuse gas (with initial temperatures and volume densities of $T = 8000$ K and $n_H = 1.5$ cm^{-3}, respectively), where cold and dense structures ($T < 100$ K and $n_H > 100$ cm^{-3}) form due to thermal instability and hydromagnetic turbulence. The initial magnetic field considered in the simulation aligns with typical values in the diffuse ISM (4 μG) and is directed along one of the main axes of the cube (hereafter, the x axis).

This model was used in P21 to simulate radio emission below 200 MHz. We follow the same recipe and derive T_b by means of Eqs. (1) and (2), where $B_\perp$ varies depending on the choice of the main axis of the cube considered for the integration of Eq. (2), and j_e is described by model A. Given the simulated T_b maps, we measure β_{syn} between 45 MHz and 408 MHz for each LOS, as done with real observations. As we do not apply any Gaussian beam to the synthetic data, the choice of θ_T does not affect the estimate of β_{syn}. From the β_{syn} maps, we interpolate back the value of $\langle B_\perp \rangle$ using model A (see Sect. 4.1) and compare it with the true median value of the simulated magnetic field along each sight line ($\tilde{B}_\perp$).

In the left panel of Fig. 5, we show the ratio between $\langle B_\perp \rangle$ and $\tilde{B}_\perp$ as a function of the latter. We explore three cases that differ in their integration axis, namely one along (plane of the sky – POS – yz) and two across (POS, xy and xz) the mean magnetic-field direction.

Our methodology generally results in an excess bias toward the actual value of $\tilde{B}_\perp$, which becomes more pronounced – changing by up to a factor of two – as the magnetic-field strength decreases. Consequently, the most severe bias arises when integrating the cube along the mean direction of the magnetic field. In the other two cases, our estimates are highly consistent (within 1σ) with the true value of the magnetic field.

In the right panel of Fig. 5, for the POS equal to the xy plane, we test the bias on the estimate of $\tilde{B}_\perp$ in the case where we misinterpret the energy flux of CRe. While always considering model A in the synthetic data, we interpolate back $\langle B_\perp \rangle$ referring to the models of Padovani et al. (2018) and Orlando (2018) in teal and purple, respectively. As expected from Fig. 2, both cases significantly overestimate $\tilde{B}_\perp$ compared to model A, reaching excess biases of more than one order of magnitude in the case of Padovani et al. (2018).

5. Discussion

We introduce a new analytical model for j_e that depends on a minimal set of parameters, making it easily usable for modeling the diffuse synchrotron emission of the Galaxy. Nevertheless, it is important to clarify that our phenomenological model does not represent the injection spectrum of CRe at the emission source; instead, it corresponds to the effective CRe spectrum after propagation and attenuation processes.

We shown that, over most of the sky, j_e can be considered to be relatively spatially uniform (at least at the angular scales probed by this work). A set of model parameters (see model A in Table 1) can be chosen such that the values of $\langle B_\perp \rangle$ needed to reproduce available β_{obs} at low frequencies are broadly consistent with the magnetic-field strength measured in the diffuse ISM below 10 μG (e.g., Heiles & Troland 2005; Sobey et al. 2019). This is displayed in the all-sky map of $\langle B_\perp \rangle$ shown in Fig. 4. However, a few structures coinciding with known arcs in the radio sky seem to distinguish themselves from the average trend with anomalously large values of $\langle B_\perp \rangle$. The origin of these structures is highly debated (e.g., Sofue 2015; Kataoka et al. 2021; Panopoulou et al. 2021). They could represent the relic of several supernova remnants, which may affect the energy distribution of CRe in the presence of stronger and compressed magnetic fields (e.g., Morlino & Celli 2021). As an example, in Fig. 6, we show

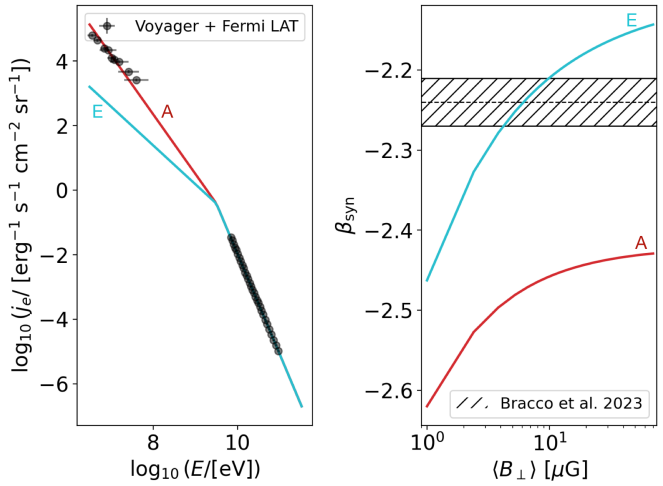

Fig. 6. Same as in the left and right panels of Fig. 2 but for the observed values of β_{obs} in the Orion-Taurus ridge in hatches (Bracco et al. 2023). Models A and E for β_{syn} (right) and j_{e} (left) are overlaid in red and cyan lines, respectively (see Table 1).

the same as in Fig. 2 but for the β_{obs} values measured by Bracco et al. (2023) in one radio arc, namely the Ori-Tau ridge. In this case, it is not possible to reproduce the observations between −2.3 and −2.2 using model A unless resorting to $\langle B_\perp \rangle$ values of hundreds of μG. Conversely, the range of β_{obs} in the Ori-Tau ridge can be accounted for with more standard values of $\langle B_\perp \rangle$ using our model E in Table 1. Model E adjusts the CRe population at low energy (below 1 GeV), departing from the local ISM conditions probed by the Voyager spacecraft.

This example illustrates the versatility of our model and its ability to be tailored to various astrophysical scenarios. Such adaptability is crucial for optimizing existing modeling of synchrotron emission (e.g., Bracco et al. 2022), especially as new discoveries at low frequencies continue to emerge. For instance, our model could help us guide the interpretation of recent and unprecedented findings made with the LOFAR telescope, one of the main SKA precursors below 200 MHz (e.g., Zaroubi et al. 2015; Van Eck et al. 2017, 2019; Jelić et al. 2018; Bracco et al. 2020; Turić et al. 2021). These observations highlight the unexpected correlation between synchrotron polarization – which is affected by Faraday rotation (Ferrière et al. 2021) – and tracers of the neutral interstellar gas, paving the way to a new perspective on structure formation in the multiphase and magnetized Galactic ISM.

6. Summary

Cosmic-ray electrons (CRe) with energies of around 1 GeV are expected to be the primary contributors to the diffuse synchrotron radiation observed in the Galaxy at radio frequencies below 1 GHz. However, determining their exact energy flux (j_{e}) has proven challenging because of solar modulation occurring between 100 MeV and 10 GeV. Previous attempts to reconcile the radio nonthermal emission with j_{e} within this energy range have been successful, but require unexpectedly large values for the average Galactic magnetic-field strength perpendicular to the sight line ($\langle B_\perp \rangle$).

In this work, we introduce a new analytical model for j_{e} capable of fitting ancillary data for the CRe energy flux (i.e., Voyager and *Fermi*-LAT) while meeting observational constraints on the spectral index of the brightness temperature at low frequencies, denoted β_{obs}. The model achieves this while maintaining values of $\langle B_\perp \rangle$ that are consistent with existing measurements in the diffuse ISM below 10 μG (e.g., Crutcher 2012). We used the β_{obs} map obtained between 45 MHz and 408 MHz by G11, found the best model that reproduces these observations, and validated its performance against various measurements of β_{obs} in the literature between 50 MHz and 1 GHz.

Our fiducial model (model A in Table 1) allows us to derive, for the first time, an all-sky map of $\langle B_\perp \rangle$; we tested this map against synthetic data of synchrotron emission produced from state-of-the-art MHD simulations of the multiphase and magnetized ISM.

We find that, up to angular scales of a degree level, a uniform spatial distribution of j_{e} can be assumed for diffuse emission at intermediate-to-high Galactic latitudes. Only a few regions in the sky are at variance with the average trend; these correspond to known arc-like structures in the radio band. We demonstrate the versatility of our model to account for these anomalous regions in the case of the Orion-Taurus ridge (Bracco et al. 2023).

This work represents a useful step forward in modeling Galactic diffuse emission at low frequency given the adaptability of our data-driven four-parameter model of j_{e}. It marks an important milestone in the interpretation of current low-frequency observations of the diffuse ISM, such as those from the LOFAR telescope, and will help in future analyses, with the SKA coming online.

Acknowledgements. We express our gratitude to the referee, Andy Strong, whose comments improved the quality of this manuscript. We are grateful to Elena Bellomi, Benjamin Godard, and Patrick Hennebelle for providing us with the MHD simulations that were used to generate synthetic data of synchrotron emission. We are thankful to Marta Spinelli for discussions on low-frequency observations of the synchrotron spectral index. A.B. acknowledges financial support from the INAF initiative "IAF Astronomy Fellowships in Italy" (grant name MEGASKAT). In the analysis we made use of `astropy` (Astropy Collaboration 2018), `scipy` (Virtanen et al. 2020), and `numpy` (Harris et al. 2020).

References

Ackermann, M., Ajello, M., Atwood, W. B., et al. 2010, Phys. Rev. D, 82, 092004
Adriani, O., Barbarino, G. C., Bazilevskaya, G. A., et al. 2011, ApJ, 742, 102
Aguilar, M., Aisa, D., Alvino, A., et al. 2014, Phys. Rev. Lett., 113, 121102
Alvarez, H., Aparici, J., May, J., & Olmos, F. 1997, A&AS, 124, 205
Astropy Collaboration (Price-Whelan, A. M., et al.) 2018, AJ, 156, 123
Bellomi, E., Godard, B., Hennebelle, P., et al. 2020, A&A, 643, A36
Bowman, J. D., Rogers, A. E. E., & Hewitt, J. N. 2008, ApJ, 676, 1
Bracco, A., Jelić, V., Marchal, A., et al. 2020, A&A, 644, A3
Bracco, A., Ntormousi, E., Jelić, V., et al. 2022, A&A, 663, A37
Bracco, A., Padovani, M., & Soler, J. D. 2023, A&A, 677, A11
Bridle, A. H. 1967, MNRAS, 136, 219
Crutcher, R. M. 2012, ARA&A, 50, 29
Cummings, A. C., Stone, E. C., Heikkila, B. C., et al. 2016, ApJ, 831, 18
Dewdney, P. E., Hall, P. J., Schilizzi, R. T., & Lazio, T. J. L. W. 2009, IEEE Proc., 97, 1482
Dowell, J., Taylor, G. B., Schinzel, F. K., Kassim, N. E., & Stovall, K. 2017, MNRAS, 469, 4537
Ferrière, K., West, J. L., & Jaffe, T. R. 2021, MNRAS, 507, 4968
Fromang, S., Hennebelle, P., & Teyssier, R. 2006, A&A, 457, 371
Gabici, S. 2022, A&A Rev., 30, 4
Ginzburg, V. L., & Syrovatskii, S. I. 1964, The Origin of Cosmic Rays (New York: Macmillan)
Guzmán, A. E., May, J., Alvarez, H., & Maeda, K. 2011, A&A, 525, A138
Harris, C. R., Millman, K. J., van der Walt, S. J., et al. 2020, Nature, 585, 357
Haslam, C. G. T., Salter, C. J., Stoffel, H., & Wilson, W. E. 1982, A&AS, 47, 1
Heald, G., Mao, S. A., Vacca, V., et al. 2020, Galaxies, 8, 53
Heiles, C., & Troland, T. H. 2005, ApJ, 624, 773
Irfan, M. O., Bull, P., Santos, M. G., et al. 2022, MNRAS, 509, 4923
Jelić, V., Prelogović, D., Haverkorn, M., Remeijn, J., & Klindžić, D. 2018, A&A, 615, A3
Jones, M. E., Taylor, A. C., Aich, M., et al. 2018, MNRAS, 480, 3224

Kataoka, J., Yamamoto, M., Nakamura, Y., et al. 2021, ApJ, 908, 14
Longair, M. S. 2011, High Energy Astrophysics (Cambridge, UK: Cambridge University Press)
Maeda, K., Alvarez, H., Aparici, J., May, J., & Reich, P. 1999, A&AS, 140, 145
Morlino, G., & Celli, S. 2021, MNRAS, 508, 6142
Mozdzen, T. J., Bowman, J. D., Monsalve, R. A., & Rogers, A. E. E. 2017, MNRAS, 464, 4995
Mozdzen, T. J., Mahesh, N., Monsalve, R. A., Rogers, A. E. E., & Bowman, J. D. 2019, MNRAS, 483, 4411
Mulcahy, D. D., Horneffer, A., Beck, R., et al. 2018, A&A, 615, A98
Orlando, E. 2018, MNRAS, 475, 2724
Padovani, M., & Galli, D. 2018, A&A, 620, L4
Padovani, M., Galli, D., Ivlev, A. V., Caselli, P., & Ferrara, A. 2018, A&A, 619, A144
Padovani, M., Bracco, A., Jelić, V., Galli, D., & Bellomi, E. 2021, A&A, 651, A116
Panopoulou, G. V., Dickinson, C., Readhead, A. C. S., Pearson, T. J., & Peel, M. W. 2021, ApJ, 922, 210
Planck Collaboration XXV. 2016, A&A, 594, A25
Ponnada, S. B., Panopoulou, G. V., Butsky, I. S., et al. 2024, MNRAS, 527, 11707
Porter, T. A., Jóhannesson, G., & Moskalenko, I. V. 2022, ApJS, 262, 30
Price, D. C., Greenhill, L. J., Fialkov, A., et al. 2018, MNRAS, 478, 4193
Reich, P., & Reich, W. 1988a, A&AS, 74, 7
Reich, P., & Reich, W. 1988b, A&A, 196, 211
Reissl, S., Brauer, R., Klessen, R. S., & Pellegrini, E. W. 2019, ApJ, 885, 15
Rockstroh, J. M., & Webber, W. R. 1978, ApJ, 224, 677
Roger, R. S., Costain, C. H., Landecker, T. L., & Swerdlyk, C. M. 1999, A&AS, 137, 7
Rybicki, G. B., & Lightman, A. P. 1979, Radiative processes in astrophysics (New York: Wiley)
Sathyanarayana Rao, M., Subrahmanyan, R., Udaya Shankar, N., & Chluba, J. 2017, ApJ, 840, 33
Sironi, G. 1974, MNRAS, 166, 345
Sobey, C., Bilous, A. V., Grießmeier, J. M., et al. 2019, MNRAS, 484, 3646
Sofue, Y. 2015, MNRAS, 447, 3824
Spinelli, M., Bernardi, G., Garsden, H., et al. 2021, MNRAS, 505, 1575
Stanislavsky, L. A., Bubnov, I. N., Konovalenko, A. A., Stanislavsky, A. A., & Yerin, S. N. 2023, A&A, 670, A157
Stone, E. C., Cummings, A. C., Heikkila, B. C., & Lal, N. 2019, Nat. Astron., 3, 1013
Strong, A. W. 1977, MNRAS, 181, 311
Strong, A. W., & Wolfendale, A. W. 1978, J. Phys. G Nucl. Phys., 4, 1793
Strong, A. W., Moskalenko, I. V., & Reimer, O. 2000, ApJ, 537, 763
Sun, X. H., Reich, W., Waelkens, A., & Enßlin, T. A. 2008, A&A, 477, 573
Teyssier, R. 2002, A&A, 385, 337
Turić, L., Jelić, V., Jaspers, R., et al. 2021, A&A, 654, A5
Unger, M., & Farrar, G. R. 2024, ApJ, 962, L5
Van Eck, C. L., Haverkorn, M., Alves, M. I. R., et al. 2017, A&A, 597, A98
Van Eck, C. L., Haverkorn, M., Alves, M. I. R., et al. 2019, A&A, 623, A71
van Haarlem, M. P., Wise, M. W., Gunst, A. W., et al. 2013, A&A, 556, A2
Vidal, M., Dickinson, C., Davies, R. D., & Leahy, J. P. 2015, MNRAS, 452, 656
Virtanen, P., Gommers, R., Oliphant, T. E., et al. 2020, Nat. Methods, 17, 261
Waelkens, A., Jaffe, T., Reinecke, M., Kitaura, F. S., & Enßlin, T. A. 2009, A&A, 495, 697
Wang, J., Jaffe, T. R., Enßlin, T. A., et al. 2020, ApJS, 247, 18
Webster, A. 1975, MNRAS, 171, 243
Zarka, P., Girard, J. N., Tagger, M., & Denis, L. 2012, in SF2A-2012: Proceedings of the Annual meeting of the French Society of Astronomy and Astrophysics, eds. S. Boissier, P. de Laverny, N. Nardetto, et al., 687
Zaroubi, S., Jelic, V., de Bruyn, A. G., et al. 2015, MNRAS, 454, L46